Visible light driven hydrogen evolution by photocatalytic reforming of lignin and lactic acid using one-dimensional NiS/CdS nanostructures

Chunhe Li[a], Hongmei Wang[b,c,*], Sara Bonabi Naghadeh[c], Jin Zhong Zhang[c], Pengfei Fang[a,*]

[a] Department of Physics and Hubei Nuclear Solid Physics Key Laboratory, Wuhan University, Wuhan, 430072, China
[b] College of Biological, Chemical Sciences and Engineering, Jiaxing University, Jiaxing, 314001, China
[c] Department of Chemistry and Biochemistry, University of California, Santa Cruz, CA, 2306, 95064, USA

A B S T R A C T

Uniform one-dimensional (1D) NiS/CdS nanocomposites have been fabricated using CdS nanowires (NWs) and NiS nanoparticles as building blocks through two-pot solvothermal synthesis. The synergistic interaction between CdS and NiS, stemming from their intimate contact, efficiently enhanced charge carrier separation, with the NiS, as a non-noble metal cocatalyst, enriching the active sites for H_2 production from water. Consequently, compared with pristine CdS NWs, the 1D NiS/CdS nanocomposite exhibited improved visible light reactivity in the generation of H_2. The activity of NiS/CdS with 20 mol% of NiS loading, under the coexistence of lactic acid and lignin as hole scavengers, is 5041 times that of pristine CdS, with an apparent quantum efficiency (AQE) of 44.9% for H_2 generation. To gain deeper insight into the mechanism behind the enhanced performance, ultrafast dynamics studies based on femtosecond transient absorption (TA) techniques have been applied to probe the charge carrier dynamics. The results reveal that presence of 0.2 molar ratio of NiS improved the average charge carrier lifetime of CdS NWs by 97 times, potentially leading to more efficient charge separation and transfer. However, further increasing the NiS loading resulted in shorter lifetime or faster electron-hole recombination, attributed to aggregation of NiS nanoparticles. The dynamics results agree well with the photocatalytic results in that the longer charge carrier lifetime correlates with improved performance in hydrogen evolution. This work demonstrates a simple approach to controlled synthesis of well-shaped 1D nanocomposite photocatalysts for visible-light driven energy conversion, particularly involving the use of biomass.

1. Introduction

Hydrogen energy is an ideal alternative to fossil fuels and is predicted to play an indispensable role in renewable energy technologies in the future [1,2]. Enlightened by natural photosynthesis, varieties of semiconductors, for instance nitrides [3], metal-organic frameworks (MOFs) [4,5], TiO_2 or ZnO based photocatalysts [6,7], and (oxy) sulfides [8–11], have been widely researched as photon absorbers and photocatalysts in artificial light driven water splitting for hydrogen evolution reaction (HER). Among them, CdS is attractive on account of its wanted bandgap (2.4 eV) and matching band-edge stations [12]. Nevertheless, CdS has two limitations. First, its photocatalytic efficiency is seriously confined by rapid recombination of photogenerated charge carriers [13]. Second, CdS is subjected to photocorrosion under light irradiation, with S^{2-} in CdS self-oxidized by photoinduced holes instead of the oxidation of others [14]. Therefore, attempt have been made to either reduce recombination rate of charge carriers or prevent self-photocorrosion of CdS, such as doping or modifying with other

semiconductors [15,16]. Among kinds of strategies, co-catalyst decoration is one of the most effective ways [17–21]. In particular, noble metals have been proved to be efficient co-catalysts for HER. However, the high price of noble metals limits their applications in practice. Therefore, it is urgent to exploit inexpensive, non-noble metal-based, and valid co-catalysts for HER.

Nickel sulfide (NiS), a *p*-type semiconductor, has caused increasing concern because of its low-cost, good electrical properties, and other unique property such as highly electrocatalytic effect toward the polysulfide reaction [22,23]. For example, Zhang et al. prepared NiS modified TiO_2 using solvothermal method for the photocatalytic H_2 production with an evolution rate of 0.7 mmol h^{-1} g^{-1} [24]. Chen et al. synthesized g-C_3N_4/NiS hybrid photocatalysts through in situ template-free ion-exchange process with H_2 production rate of 0.45 mmol h^{-1} g^{-1} [25]. Furthermore, Xu et al. found that NiS can be employed to cocatalyst of CdS for photocatalytic water splitting from lactic sacrificial solution via a simple hydrothermal method, and the H_2 evolution rate reached 2.8 mmol h^{-1} [26]. Yu et al. developed NiS

nanoparticle decorated CdS nanorods photocatalysts using a convenient two-step hydrothermal approach, with an H$_2$ evolution rate of 1.13 mmol h^{-1} g^{-1} [27]. As far as we know, 1D NiS/CdS nanowire composite has yet to be applied to HER.

In the meantime, the water-splitting process is inherently unfavorable thermodynamicallly, and rapid reaction between O$_2$ and H$_2$ produced limited hydrogen production [28]. For the sake of address these topics, one approach is to put in sacrificial agents to expend the oxygen-derived groups generated, preventing subsequent O$_2$ production and its reverse reaction with H$_2$. Besides, the sacrificial agents serve as hole scavengers, increasing the separation efficiency of electrons and holes. One ideal scenario to address these issues is by photoreforming of alcohols in the photocatalytic HER. The photoreforming of alcohols, for example methanol [2,29], ethanol [30] or glycerol [31], has been completely investigated over the past decade. These alcohols are classified the first generation of biofuels, as they are derived from biomass, for example starches, sugars, or vegetable oils. Yet the consumption of these substances as a hydrogen precursor threatens with their application as food. Therefore, the utilization of lignocellulosic biomass has been paid high attention to the second generation of biofuels, for they can be planted in combination with crop or on barren soil. Lignocellulose contains three main biopolymers, that is lignin (15–20%), hemicellulose (25–35%) and cellulose (40–50%) [32]. Lignin is the most stubborn of the three components of lignocellulosic biomass. Bled by paper industries and pulp as discards from wood and crude materials, lignin results in the pulp and paper wastewater tough to deal with conventional wastewater treatment technology. Therefore, if lignin could also serve as sacrificial agents (hole scavengers) to reduce the rate of charge carrier recombination, the photocatalytic method for degradation of lignin can be used in conjunction with the production of hydrogen from water splitting. Nevertheless, this approach has not been extensively investigated previously.

In this work, we fabricated 1D NiS/CdS nanocomposites using a two-step solvothermal method. The nanocomposite shows obviously enhanced HER activity compared with pure CdS nanowires (NWs). The H$_2$ evolution rate obtained using the optimized photocatalyst is up to 147.7 µmol h^{-1} g^{-1} (λ ≥ 400 nm) and the apparent quantum efficiency (AQE) was 44.9% from aqueous solution of lignin and lactic acid. The stronger light absorption and more efficient electron transfer of the nanocomposites are confirmed by UV–vis spectroscopy and the photoelectrochemical properties, which could lead to the enhanced photocatalytic water splitting ability in comparison with that of pristine CdS. Furthermore, the effect of the NiS loading on charge carrier dynamics has been researched using femtosecond transient absorption (TA) spectroscopy, which offers information about charge separation and transfer from CdS to NiS. These results prove that the appropriate amount of loading of NiS can substantially enhance charge carrier separation and transfer, correlating with significant enhancement in the photocurrent density. This work demonstrates the potential of NiS/CdS nanocomposite as an effective photocatalyst for hydrogen evolution utilizing lignocellulosic biomass.

2. Experimental section

2.1. Materials

All the chemical reagents used in the experiment were provided by Sinopharm Chemical Reagent Co., Ltd, Shanghai without further purification. Deionized water was employed in all the experiments throughout.

2.2. Material synthesis

The 1D NiS/CdS nanonanocomposites were assembled by a template-free and mild two-step solvothermal method. The first step was the fabricate CdS NWs. In a typical process, cadmium

diethyldithiocarbamate (Cd(S$_2$CNEt$_2$)$_2$), prepared by sediment from a stoichiometric precursor mixture of cadmium chloride (0.01 mol) and sodium diethyldithiocarbamate trihydrate (0.01 mol) in 50 mL of deionized water, was transferred to a Teflon-lined stainless steel autoclave. Then, the autoclave was filled with 40 mL of ethylenediamine. The autoclave was heated at 180 °C for 24 h and then cooled down to room temperature. The pale yellow sediment was collected and washed several times with absolute ethanol and deionized water. The final products were dried in a vacuum oven at 60 °C for 12 h.

The second step was to fabricate 1D NiS/CdS nanocomposites. The above prepared CdS NWs were ultrasonically dispersed in 70 mL of ethylene glycol solution containing nickel nitrate (0.58 g) and thiourea (0.3 g). Then the solution was transferred into a 100 mL stainless steel autoclave and heated at 180 °C for 12 h after stirring for 0.5 h. The obtained precipitates were collected by centrifugation, washed with deionized water before being dried in a vacuum oven at 60 °C. The molar ratio of NiS and CdS was varied (0.1, 0.2, 0.4, 0.6, 0.8 and 1.0) by adjusting the CdS amount.

2.3. Characterization

The morphologies of the samples were determined with scanning electron microscopy (SEM, Hitachi S-4800), transmission electron microscopy (TEM, JEOL TEM-2010) and high-resolution transmission electron microscopy (HRTEM, JEM-2010 FEM). Elemental analysis of the photocatalysts was conducted by an energy dispersive X-ray spectrometer (EDS) attached to TEM. The crystal phases of the samples were characterized with a Bruker D8-advance X-ray diffraction (XRD), performed on with Cu Kα radiation. The results were obtained at a scanning speed of 4° steps over the 2θ ranged from 20° to 80°, and the accelerating voltage and operating current were 40 kV and 40 mA, respectively. The specific surface areas were measured by BET method utilizing nitrogen adsorption-desorption apparatus (JW-BK122W, China). The pore volume and distribution were determined by the Barrett, Joyner, and Halenda (BJH) method. The X-ray photoelectron spectroscopy (XPS,) was conducted with Thermo 163 Fisher ESCALAB 250Xi. UV–vis diffuse reflectance spectra (DRS) were collected with a Shimadzu UV-2550 spectrometer with BaSO$_4$-coated integration sphere. Fourier-transform infrared (FT-IR) spectra were determined by using a Thermo Fisher Nicolet iS10 Fourier-transform infrared spectrometer. Inductively coupled plasma mass spectrometry (ICP-MS) was recorded on a PerkinElmer 350 D instrument.

2.4. The evaluation of photocatalytic hydrogen production

Photocatalytic hydrogen production test was evaluated in an air-tight glass reactor with high transparent quartz on top of the glass cover. Before all experiments, 0.100 g sample was added into 100 mL solution (including different sacrificial agent). The sample was treated with ultrasonication for 10 min and then the whole equipment was evacuated with vacuum pump for 0.5 h to exhaust the air as well as establish adsorption-desorption equilibrium in the reactor. The reaction mixture was stirred gently, and the reaction temperature was kept at room temperature by cooling water circulation system. A 300 W Xe lamp with a cutoff filter (≥ 400 nm) was irradiated from the top of glass reactor. The gaseous H$_2$ was periodically extracted from the hydrogen production device and measured by gas chromatograph (CEL-GC7900), assembled with a thermal conductivity detector (TCD), ultrapure nitrogen as carrier gas. The gases generated in the reaction were quantified with standard curve of H$_2$ gas. The AQE of H$_2$ production was performed under the same photocatalytic conditions. The AQE was estimated by the following equation.

$$AQE\,[\%] = \frac{number\ of\ reacted\ electrons}{number\ of\ incident\ photons} \times 100$$

$$= \frac{number\ of\ H_2\ molecules \times 2}{number\ of\ incident\ photons} \times 100$$

2.5. Photoelectrochemical measurements

The experiments were proceeded using an electrochemical workstation (CHI-660D, Chen Hua, China). A 300 W Xe lamp equipped with a 400 nm cut-off filter as the visible-light lamp. The distance between the photoelectric reaction cell and Xe lamp was 20 cm. The working electrode was made as follows: 10 mg sample was dispersed into 1.0 mL anhydrous ethanol to make a slurry. The electrodes were made using the slurry spin-coating onto an indium-tin oxide (ITO) glass substrate (1 cm × 2 cm) and then naturally air dried.

Photoelectrochemical activities of samples were measured in three-electrode quartz cell with $0.10\ mol\,L^{-1}$ KCl, $0.10\ g\,L^{-1}$ lignin and 2.0 vol% lactic acid electrolyte solution using the prepared film electrodes as working electrodes, Platinum electrode as counter electrode and a saturated Ag/AgCl as reference electrode, respectively.

2.6. Ultrafast transient absorption spectroscopy

The femtosecond transient absorption measurements were carried using a Quantronix laser system as described previously [33]. Briefly, the system consists of an Er-doped fiber oscillator, regenerative amplifier and diode-pumped Nd:YLF pump laser (527 nm). The amplified beam splits in a 1:9 ratio to generate a white light continuum probe pulse (450–750 nm) and feed an optical parametric amplifier respectively. All the sample were photoexcited using 390 nm beam with various pulse energies (750, 323 and 190 nJ/pulse) to study power dependence in the samples. The pump and probe overlapped on the sample spatially and temporally. The transient absorption data was collected using a charge-coupled device (CCD) detector over a temporal delay interval of 0–1000 ps between the pump and probe pulses.

3. Results and discussion

3.1. Structure, composition, and optical properties of photocatalysts

The morphologies of CdS and 0.2-NiS/CdS nanocomposite were investigated using SEM. As shown in Fig. S1a-b, the pure CdS exhibits uniform and smooth 1D nanowire structures with an average diameter of about 50–90 nm and a length of several hundred nanometers. Fig. S1c-d shows the 0.2-NiS/CdS nanocomposite that still maintains the 1D nanowire structure, but their average diameter is a little larger than that of pristine CdS and surface becomes rougher along the entire nanowires due to NiS nanoparticles tightly coated onto the CdS NWs. It is anticipated that the CdS NWs provide affluent highly accessible active site of the interfaces for the growth of NiS.

To more precisely determine the feature and microstructure of the CdS and NiS/CdS nanocomposites, TEM has been employed. As shown in Fig. 1a,b, the pure CdS exhibits the smooth surface and highly uniform 1D structure with a diameter of 82.4 nm, which is accordance with the SEM results. The HRTEM (inset in Fig. 1b) confirms that pure CdS MWs show lattice fringes with lattice spacing of 0.24 nm, which matches with the (100) plane of CdS. The nearly perfect lattice fringes of the CdS in the HRTEM images demonstrate that the synthesized CdS is of high crystallinity. Fig. 1c–d show the TEM morphology of 0.2-NiS/CdS nanocomposite. The EDS inset in Fig. 1c demonstrates the presence of Cd, S and Ni elements, indicating the coexistence of NiS and CdS. Because lacey support films are used to support the samples, the elements C and Cu can be observed from EDS. The O element may be from the surface-adsorbed oxygen species. It is also clear that the 1D CdS is wrapped by NiS nanoparticles. The NiS appeared as irregular

nanoparticles with the size about 30 nm and lattice distance of 0.29 nm, corresponding to the (300) plane of NiS [34]. The NiS nanoparticles are attached on the surface of CdS NWs. Further increasing the molar ratio of NiS and CdS to 1.0 (as shown in Fig. 1e–f), all of the CdS NWs are covered by excessive NiS nanoparticles, which themselves began to agglomerate. Fig. 1g–h show the HRTEM images of 1.0-NiS/CdS. The lattice fringes on NiS nanoparticles are not continuous in long-range and some amorphous features are found, indicating that it is partially crystalline NiS nanoparticles. The close look at the interface of NiS nanoparticle and CdS nanowire shows that the continuous lattice fringes of NiS directly connected to the continuous lattice fringes of CdS, implying an intimate contact between NiS and CdS, which could facilitate separation and migration of charge carriers, and thereby enhance the HER activity.

X-ray diffraction patterns was used to determine the crystallization and phase purity of the pure CdS NWs and the NiS/CdS composites with various loading amount of NiS, as shown in Fig. 2. Those peaks marked with "*" mean CdS, while the others marked with "◆" mean NiS. For the pure CdS sample, the observed peaks fit well with hexagonal phase (JCPDS No. 65-3414), revealing no impurities. After formation of the NiS/CdS nanocomposites, there was no obvious diffraction peaks for NiS when the ratio of NiS and CdS is less than 0.6, which can be attributed to the small quantity of NiS or highly dispersed the NiS including amorphous structures. Further increasing the ratio to 0.8 and then 1.0, some weak peaks can be certified as the rhombohedral millerite β-NiS phase (JCPDS No. 12-0041). Besides, there is no noticeable shift of all diffraction peaks, indicating that the change of the lattice constants of CdS nanocrystals is negligible.

Specific surface areas of photocatalysts were characterized from the nitrogen adsorption at liquid nitrogen condition using Brunauer-Emmett-Teller method. Nitrogen adsorption-desorption isotherms along with pore size distribution curves are shown in Fig. 3. These isotherms revealed the distinct type IV patterns with the H3 hysteresis loop at the P/P_0 range of 0.5–1.0 according to IUPAC, which was characteristic of mesoporous-assembled materials [35]. Fig. 3b shows the pore size distribution computed according to the adsorption embranchment of the isotherms. These mesopores may be the result of excessive NiS nanoparticles accumulating on the surface of CdS NWs. Meanwhile, the obtained S_{BET} and pore volume of NiS/CdS nanocomposites are larger than that of pure CdS NWs (shown in Table S1). This is because the irregular NiS nanoparticles grow on the surface of the CdS NWs, resulting in expanded surface area and pore volumes. Additionally, the average pore diameter of the pure CdS NWs is amaller than that of NiS/CdS nanocomposite, indicating that a number of new mesopores were formed in the NiS/CdS nanocomposite. In general, a larger surface area can afford more active sites for the photocatalytic hydrogen production. The mesoporous structures can promote the transport between the hole scavengers and their products, which favor the photocatalytic hydrogen production consequently [36,37].

XPS analysis was used to further gain insight into the chemical composition of photocatalysts. Fig. 4a shows the XPS survey spectra of the rustic CdS NWs and 0.2-NiS/CdS nanocomposite, respectively. Both samples show the main peaks of the elements Cd and S. The C1s peak is used as calibration of the binding energy and the O element detected may be from water molecules physically adsorbed on the surface of the photocatalysts. Additionally, the Ni element can be found in the 0.2-NiS/CdS nanocomposite. The characteristic high-resolution XPS of Cd 3d (Fig. 4b) for 0.2-NiS/CdS and pure CdS before reaction exhibit two binding energy peaks at 404.7 eV, 411.4 eV and 404.0 eV, 410.8 eV, respectively. The binding energy of Cd for NiS/CdS is slightly higher than that of pure CdS, indicating that the density of electrons in Cd decreases after growing NiS on CdS NWs. The variation in Cd bind energy of NiS/CdS suggests heterojunction formed between NiS and CdS, consistent with TEM results, and the possible existence of Cd-S-Ni at the interface between NiS and CdS. Based on the Pauling scale, the electronegativity of Cd and Ni is 1.69 and 1.91, respectively. The
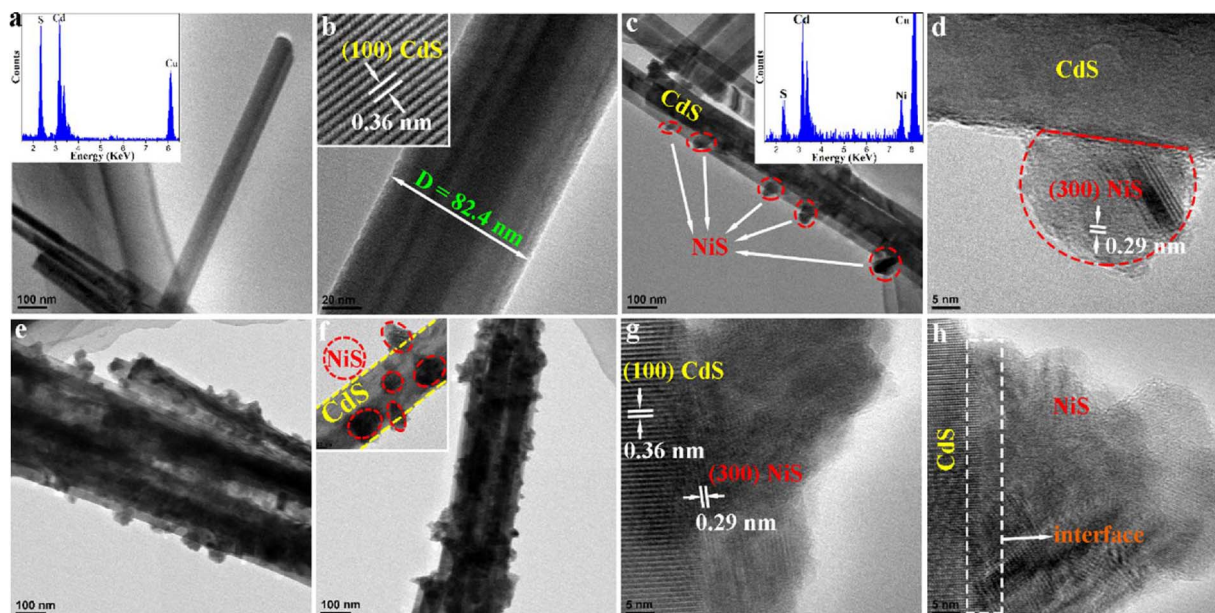
Fig. 1. a-b. TEM, EDS and HRTEM images of pure CdS; c-d. TEM, EDS and HRTEM images of 0.2-NiS/CdS nanocomposite; e-f. TEM images of 1.0-NiS/CdS nanocomposite; g-h. HRTEM image of 1.0-NiS/CdS nanocomposite.
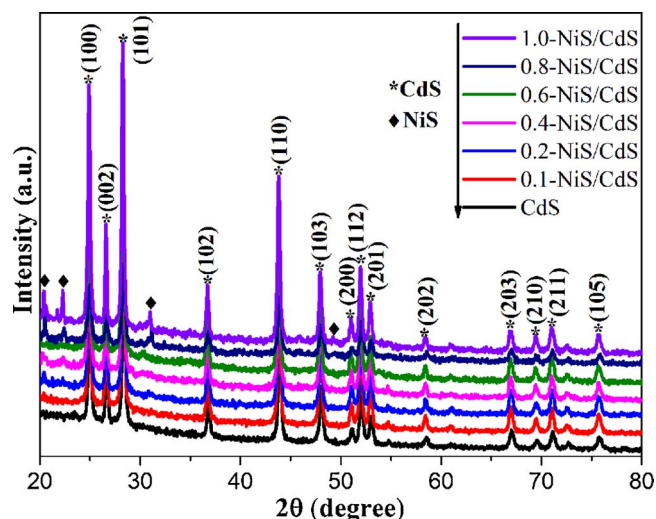

Fig. 2. XRD patterns of pure CdS and NiS/CdS nanocomposites.

electronegativity of Cd is lower than that of Ni, which results in a higher electronic density of Ni in the NiS/CdS nanocomposite and a lower electronic density of Cd. The variation of electron density for Ni and Cd implied electron transfer from CdS to NiS at the boundary [38].

When photogenerated electrons in CdS are transferred to NiS, the probability of electron-hole recombination is decreased. Fig. 4c shows the S $2p$ peaks of NiS/CdS lied in 162.3 eV and 161.1 eV, which are in accordance with S $2p_{1/2}$ and S $2p_{3/2}$ orbits, suggesting the existence of S^{2-} [39,40]. The two components ($2p_{3/2}$ = 161.8 eV, $2p_{1/2}$ = 169.4 eV) are assigned to the orbitals of S atoms in a +6 form originating from sulfate oxidized by S^{2-} [41]. The binding energy of S for NiS/CdS is also higher than that of pristine CdS. Such a shift to high binding energy suggests a strong interaction between CdS and NiS [42]. The high-resolution XPS of Ni $2p$ (Fig. 4d) shows the binding energy at 855.5 eV and 862.1 eV correspond to Ni $2p_{3/2}$ and Ni $2p_{1/2}$ in NiS [43]. The other two peaks at 861.2 eV and 879.9 eV are assigned to the satellite peaks linked to the corresponding main peak [44].

The optical performances of pure CdS and NiS/CdS nanocomposites were measured by DRS, as shown in Fig. 5. The absorption edge of pure CdS NWs is located at 514 nm, which corresponds to a bandgap of ca. 2.41 eV. After surface loading of the NiS nanoparticles, there is a small red-shift of the absorption edge. Taking the 0.2-NiS/CdS sample as an example, its absorption edge is at 528 nm, corresponding to a bandgap of ca. 2.35 eV. The red-shift of the absorption edge of the NiS/CdS nanocomposites is attributed to the tight interfacial junction between NiS and CdS and smaller intrinsic bandgap of NiS leading to the narrower band energy of NiS/CdS nanocomposites, which is beneficial for visible-light absorption [45]. From Fig. 5, the absorption edge of the NiS/CdS nanocomposites did not shift with further increasing NiS
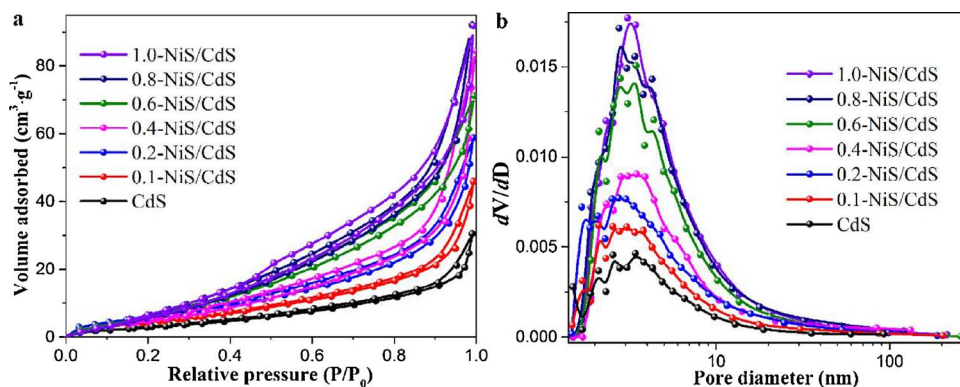

Fig. 3. a. Nitrogen adsorption-desorption isotherms; b. Pore-size distribution curves of pure CdS and NiS/CdS nanocomposites.
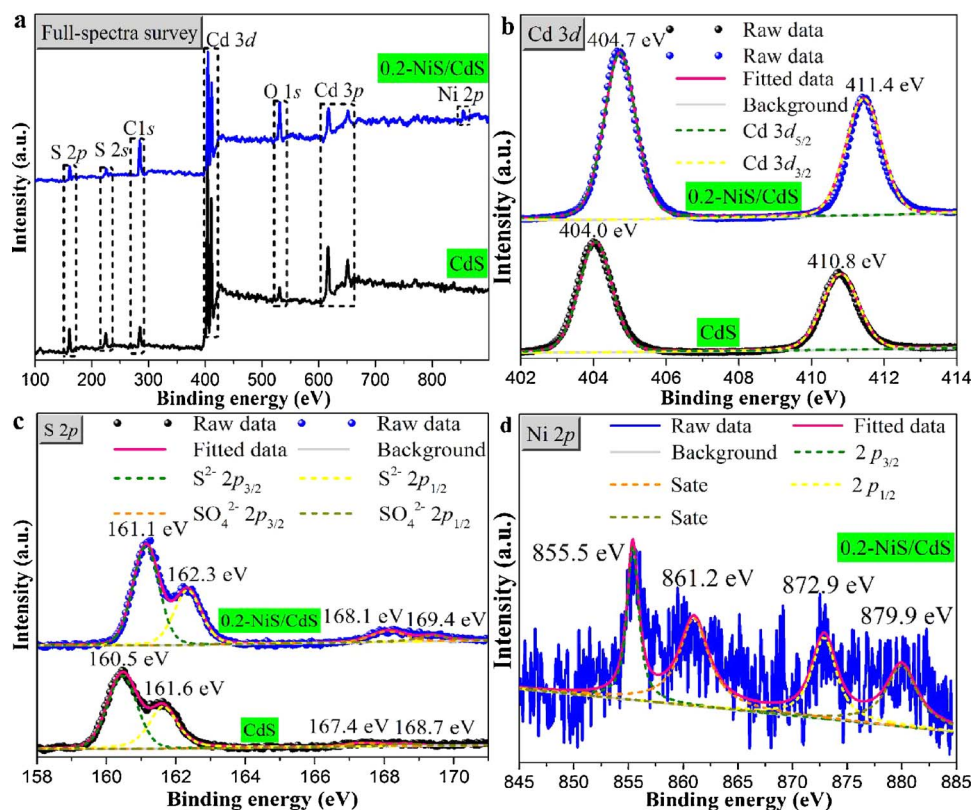
Fig. 4. a. XPS full-spectra survey of pure CdS and 0.2-NiS/CdS; b. Cd 3*d* of CdS and 0.2-NiS/CdS; c. S 2*p* of CdS and 0.2-NiS/CdS; d. Ni 2*p* of 0.2-NiS/CdS.
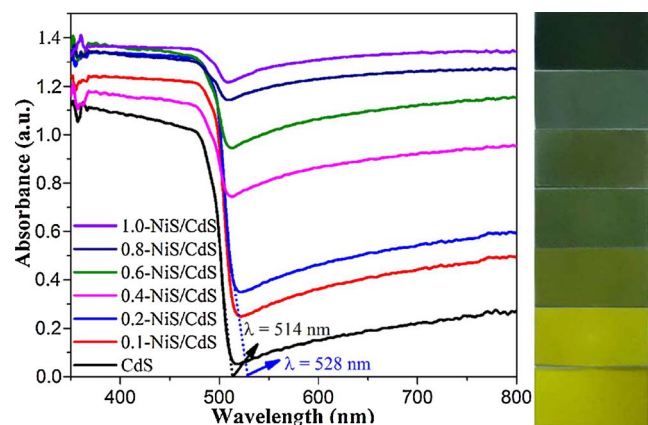

Fig. 5. UV–vis diffuse reflectance spectra (left) and thin films spin-coated ITO (right) of pure CdS and NiS/CdS nanocomposites.

content, but the absorbance becomes stronger in the visible region. The result suggests Ni^{2+} ions are not doped into CdS but grow into NiS on the surface of CdS [39]. Correspondingly, there is a distinct color change from yellow to dark green with increasing NiS content for the NiS/CdS nanocomposites (right picture in Fig. 5).

3.2. Photocatalytic H_2-evolution activity and stability of photocatalysts

Photocatalytic hydrogen production over pure CdS NWs and NiS/CdS nanocomposites were evaluated under visible light irradiation using mixed solution containing lactic acid alone or lignin and lactic acid as hole scavenger. As shown in Fig. 6, pure CdS NWs show a relatively negative photocatalytic activity during the reaction process, which is attributed to rapid recombination of photoinduced charge carriers and small number of active sites in CdS NWs. Loading NiS on the surface of CdS significantly enhanced the average rates of H_2 production. Notably, when the molar ratio of NiS and CdS is 0.2, the H_2

production rate obtains an optimal value, which is approximately 5041 or 31 times than that of CdS NWs in lignin and lactic acid or lactic acid aqueous solution, respectively. However, further increasing the amount of NiS in the nanocomposites led to a yield decrease of H_2 production, which may derive from the masking effect of NiS where the facilitated light absorption of NiS reduced the light absorption of CdS [46,47]. Comparing Fig. 6a and b show higher activity of hydrogen evolution with lignin and lactic acid used as scavenger.

The AQE for hydrogen evolution of CdS and NiS/CdS was investigated under the same reaction condition and the results were shown in Fig. 7. The trends of AQE are the same for the two different kinds of sacrificial agents and the AQE of NiS/CdS with various NiS content was higher in lignin and lactic acid aqueous solution than lactic acid alone. When the lignin and lactic acid were simultaneously chosen as sacrificial agents, the AQE of pure CdS NWs is only 0.25%. When the molar ratio of NiS and CdS is 0.1, the AQE of the NiS/CdS nanocomposite increases to 38.64%, which is 155 times higher than that of pristine CdS NWs. Meanwhile, continue increasing molar ratio of NiS and CdS to 0.2, the AQE of the NiS/CdS nanocomposite increases to 44.90%, which is 180 times higher than that of pristine CdS NWs.

The stability of photocatalysts is an important factor for HER applications. The cycling stability of the optimized sample (0.2-NiS/CdS) was measured in the presence of lignin and lactic acid every three hours, and the results are shown in Fig. 8. The 0.2-NiS/CdS nanocomposite does not show significant reduction during photocatalytic H_2 evolution for five cycles and the total amount of the hydrogen evolved for each cycle is almost the same for each cycle, which indicates that the 0.2-NiS/CdS nanocomposite has the excellent cycling stability and anti-photocorrosion ability during the photocatalytic HER under visible light. The microstructure and morphology stabilities of the 0.2-NiS/CdS nanocomposite were also demonstrated. As shown in Fig. S3, the XRD results indicate that the phases of 0.2-NiS/CdS nanocomposite showed no significant alternation after photocatalytic HER. After the durability test, the nanocomposite was further characterized by TEM. From Fig. S4 a-b, the morphology of nanocomposite showed negligible alternation

Fig. 6. The photocatalytic hydrogen production activities of different samples under visible light irradiation (λ ≥ 400 nm) in presence of lignin and lactic acid aqueous solution (a, c) and lactic acid aqueous solution (b, d), respectively.
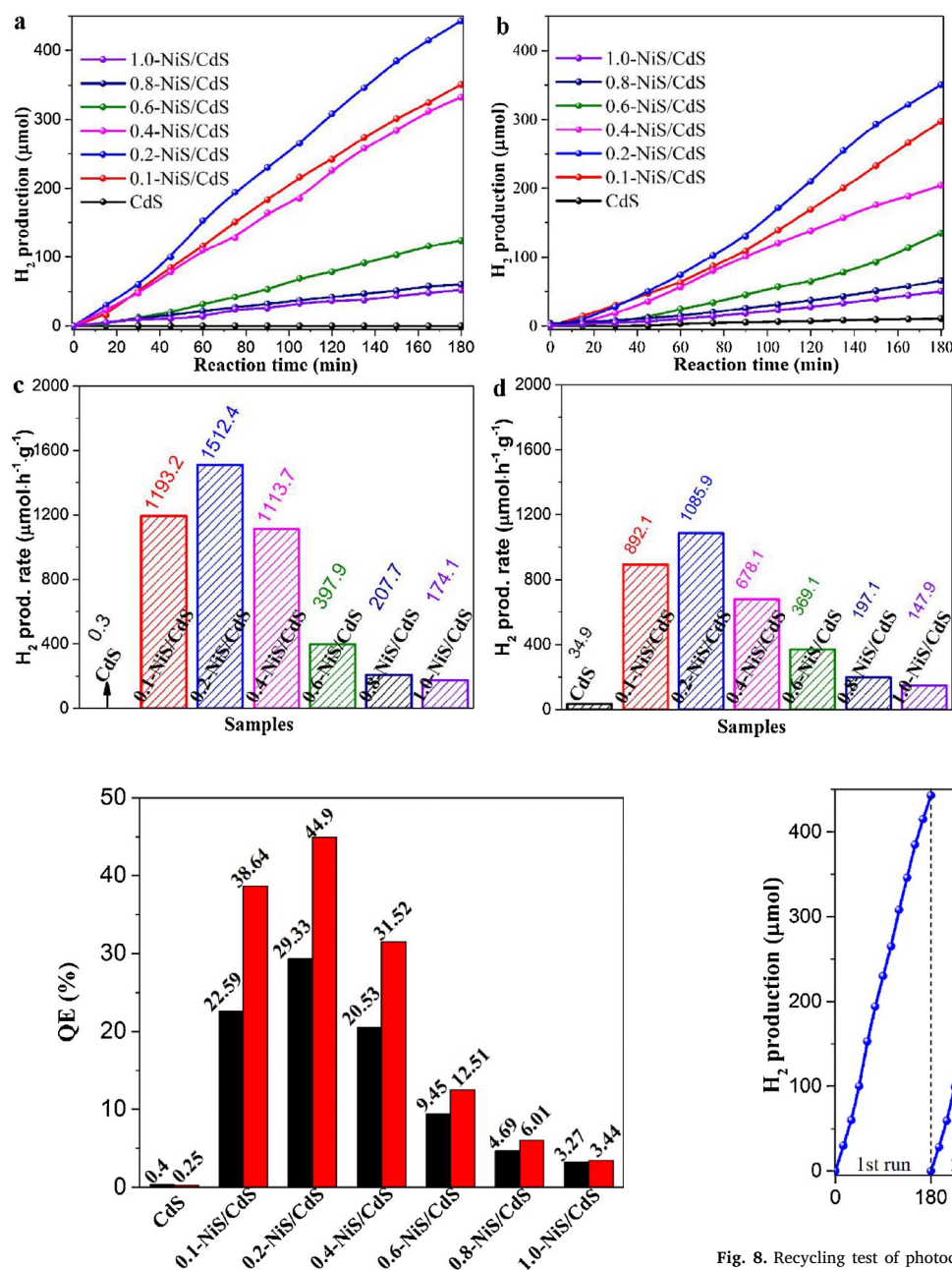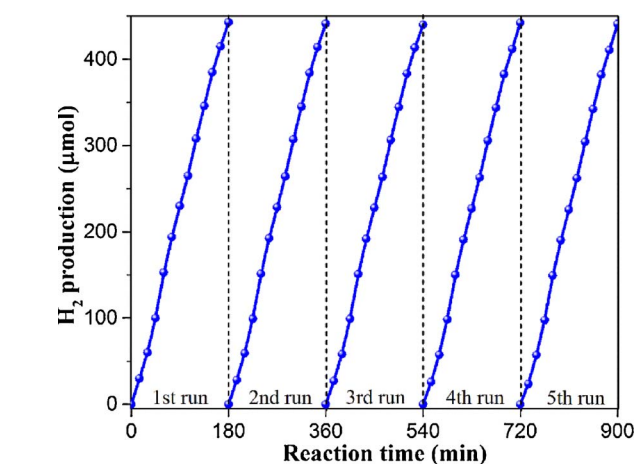

Fig. 7. Hydrogen evolution AQE of each sample in the presence of lactic acid aqueous solution (black column) and lignin and lactic acid aqueous solution (red column), respectively. (For interpretation of the references to colour in this figure legend, the reader is referred to the web version of this article.)

Fig. 8. Recycling test of photocatalytic H_2 evolution over 0.2-NiS/CdS nanocomposites under visible light irradiation (λ ≥ 400 nm) in the presence of lignin and lactic acid aqueous solution.

and many lignin nanosheets adsorbed onto its surface. And the (100) plane of CdS are still clear, indicating the absorbed lignin nanosheets are very thin. Meanwhile, as shown in Fig. S5, the XPS spectra of the nanocomposite showed no major variation in the valence state of Ni, Cd and S after photocatalytic HER, which confirms its good stability. Besides, to further verify the NiS can inhibit photocorrosion of CdS, the supernatant liquid after centrifugation of the 0.2-NiS/CdS photocatalytic system was investigated using ICP-MS. As displayed in Fig. S6, the Cd^{2+} released into the dispersion was 0.004 ppm, 0.213 ppm and 0.240 ppm, respectively. The results showed that there was only negligible Cd^{2+} in the 0.2-NiS/CdS dispersion during HER, indicating NiS efficientivly inhibit photocorrosion of CdS. All of the above results show that 0.2-NiS/CdS nanocomposite has superior HER activity and stability.

In order to investigate the content variation of lignin after HER, UV–vis spectroscopy was used to analyze lignin solution. The main absorption intensities at around 210 nm were decreased after photocatalytic hydrogen evolution for different samples, as shown in Fig. 9. The absorption peak at around 210 nm corresponds to the unsaturated chains of lignin, thereby the absorbance decrease implies the decomposition of lignin [48]. The absorption tailing to the long wavelength region arises from the color of lignin [49]. Kobayakawa et al. pointed out that lignin could be decomposed into species like methanol, ethanol, formaldehyde, formic acid and oxalic acid, which maybe contribute to hydrogen evolution [50]. As shown the inset in Fig. 9, there are different degrees of lignin degradation during hydrogen evolution using different samples. Particularly, the degradation rate of lignin reached 94% with 0.2-NiS/CdS nanocomposite. There seems to be a correlation between the lignin degradation rate and hydrogen evolution rate, indicating a possible synergistic effect between lactic acid and lignin when they are simultaneously used as sacrificial agents.
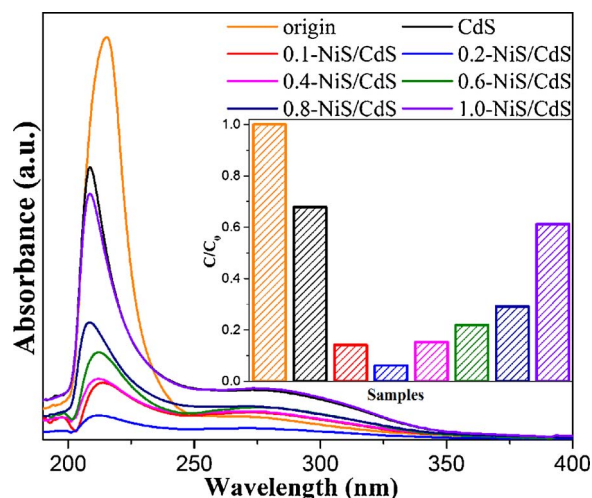
Fig. 9. Photocatalytic degradation of lignin (0.1 g L^{-1}) after hydrogen evolution using pure CdS and NiS/CdS nanocomposites.

In order to further identify the role of lignin during the HER, its morphology and structure were investigated, as shown in Fig. S7.

3.3. Photoelectrochemical study of charge separation and transfer

The photoelectrochemical performances of pure CdS and NiS/CdS nanocomposites were evaluated. Fig. 10a shows the curves of the surface photocurrent response for the different samples. The photocurrents of the photocatalysts showed the following orders: 0.2-NiS/CdS > 0.1-NiS/CdS > 0.4-NiS/CdS > 0.6-NiS/CdS > 0.8-NiS/CdS > 1.0-NiS/

CdS > CdS. The photocurrent of 0.2-NiS/CdS nanocomposite was about 9 times that of CdS, indicating higher efficient separation of photogenerated charge carrier for 0.2-NiS/CdS nanocomposite [51]. Fig. 10b shows the LSV polarization curves for bare CdS and NiS/CdS nanocomposites with various NiS content at a sweep rate 10 mV/s. Compared with pristine CdS, NiS/CdS nanocomposites show a quite higher electrocatalytic activity and the 0.2-NiS/CdS nanocomposite obtains the optimal value. This result proves that NiS loading can effectively accelerate the electrocatalytic H$_2$-evolution kinetics, consequently, enhanced the HER capability for NiS/CdS nanocomposite [52]. Fig. 10c shows the variation in electrochemical impedance spectrum (EIS) of different samples. In general, the surface charge transfer resistance was equivalent to the diameter of semicircular portion of the Nyquist diagrams and the smaller radius represents the lower resistance for charge transfer [53,54]. From Fig. 10c, NiS/CdS nanocomposites have faster interfacial electron transfer than pure CdS and the 0.2-NiS/CdS nanocomposite has the highest efficiency in separation and transfer of photoinduced charge carriers. Fig. 10d shows Bode plots of pure CdS and NiS/CdS nanocomposites. The NiS/CdS nanocomposites show improved charge separation or reduced recombination, thereby longer electron lifetime. And compared to pure CdS, the mid-frequency characteristic peak of 0.2-NiS/CdS shifts somewhat to a lower frequency (from 8.65 Hz to 4.25 Hz). The above-mentioned shift indicates a faster electron mobility process. The lifetime of electrons τ_{eff} can be extracted by the equation ($\tau_{eff} \approx 1/\omega_{min} = 1/2\pi f_{min}$) [55–57]. And the electron lifetime is only decided by the minimum frequency (ω_{min}) of the mid-frequency. In real calculation, the minimum frequency (f_{min}) of Blot plots peak is reversed as the function of electron lifetime. Particularly, the electron lifetime for the 0.2-NiS/CdS nanocomposite (59.77 ms) is around two times longer than that of pure CdS (9.2 ms). Therefore, the efficient separation and migration of photogenerated electrons between
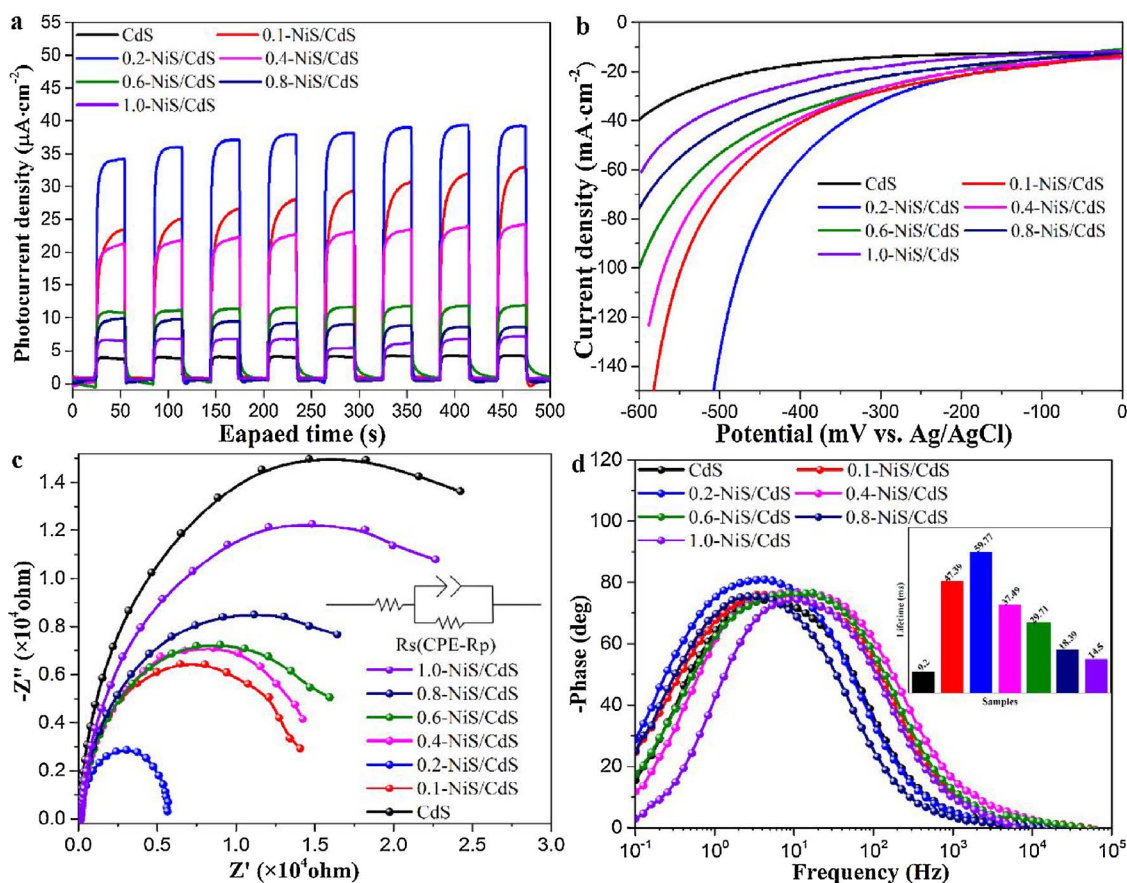

Fig. 10. a. Transient photocurrent spectra; b. LSV polarization curves; c. Electrochemical impedance spectra; d. Bode plots and lifetime (inset) for the samples utilizing 300 W Xe lamp irradiation (λ ≥ 400 nm).
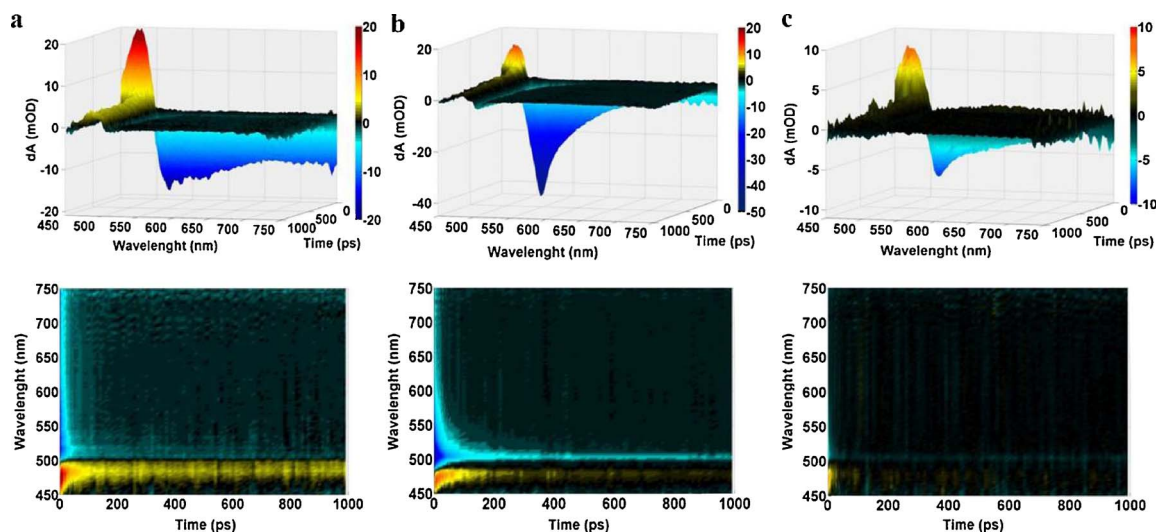
Fig. 11. 3 and 2 dimensional representation of the TA of a. CdS nanowires; b. 0.2-NiS/CdS; c. 1.0-NiS/CdS after excitation with 390 nm pump (323 nJ/pulse).

NiS and CdS facilitate the charge carrier separation, and thereby improving the corresponding activity on H_2 production.

3.4. Ultrafast studies of charge carrier dynamics

To obtain further study on charge carrier separation and transfer processes of the NiS/CdS nanocomposites, ultrafast transient absorption (TA) spectroscopy was used to explore the charge carrier dynamics in CdS NWs and their dependence on the NiS content. Fig. 11a–c shows the TA data of pure CdS, 0.2-NiS/CdS and 1.0-NiS/CdS, excited with 390 nm pump laser pulses, as a function of probe wavelength and delay time between the pump and probe pulses. The spectral profile of pure CdS and the CdS/NiS nanocomposites are mostly similar, which is due to small amount of NiS in the nanocomposite compared to CdS. The TA feature observed at 460–500 nm can be ascribed to absorption of photogenerated electrons in conduction band (CB) of CdS. The strong and broad transient bleach (TB) feature spanned from 500 to 750 nm can also be ascribed to hole absorption in the valence band (VB) of CdS as reported before [58]. The decay observed in the TB signal is ascribed to electron and hole recombination. Analyzing the decay of TB signal can provide useful insight about the behavior of the CdS with or without the NiS decorated on the surface. However, some high-order kinetic processes for instance exciton-exciton annihilation or Auger recombination can happen and interfere with correct interpretation of the data [59,60]. In order to refrain these non-linear dynamic processes, we performed pump power dependence study (750, 323 and 190 nJ/pulse) and observed slight power dependence in earlier recombination time with high pump energy (750 nJ/pulse). TA profile of each sample pumped with different energies are available in supporting information (S8). Because of the power dependence at high pump power, we chose to analyze data with pump energy of 323 nJ/pulse for comparing these three samples, which do not involve non-linear effect and have good signal to noise (S/N) ratio.

Fig. 12 shows the normalized, single wavelength ultrafast TB signals of CdS, 0.2-NiS/CdS and 1.0-NiS/CdS nanocomposites on the 0-1000 and 0-100 ps time scales. The TB signal recovery was fit with double exponential function and the fitting variables are reported in Table 1. Based on the resultant time constants, the recovery lifetime for CdS nanowires are 8.8 ± 0.4 ps and 3.6 ± 0.1 ps, for 0.2-NiS/CdS are 20 ± 1 ps and 879 ± 17 ps and for 1.0-NiS/CdS are 3.5 ± 0.1 ps and 117 ± 9 ps. According to previous studies, usually the fast time component of the decay is attributed to exciton relaxation due to presence of shallow trap states in semiconductor materials while the slower component is due to charge carrier recombination mediated by deeper

traps [61]. The average charge carrier lifetime of the samples can also be calculated using the following equation for better comparison.

$$Average\ \tau = \frac{A_1 \tau_1^2 + A_2 \tau_2^2}{A_1 \tau_1 + A_2 \tau_2}$$

The average lifetime calculated to be 8 ps, 776 ps and 76 ps for CdS, 0.2-NiS/CdS and 1.0-NiS/CdS, respectively. Based on these results, the overall charge carrier recombination is faster in CdS nanowires than 1.0-NiS/CdS and 0.2-NiS/CdS nanocomposites, respectively (CdS < 1.0-NiS/CdS < 0.2-NiS/CdS), which is in agreement with the performance of the material for HER as shown in Fig. 6. Longer charge carrier lifetime is expected to lead to better performance of the photocatalyst as the charge carriers are more likely to participate in redox reactions rather than recombining. However, as shown in Fig. 12, increasing the molar ratio of NiS from 0.2 to 1.0 caused faster recombination in earlier time regime. From the structural characterizations such as TEM images, we know that higher ratio of NiS will form aggregations on the surface of CdS NWs. Therefore, this earlier fast recombination in the 1.0-NiS/CdS nanocomposite is possibly due to charge carrier trapping by the NiS aggregates. The dynamics results seem to indicate that NiS presence on CdS NWs can improve the charge separation. However, there is an optimal ratio for efficient separation (0.2-NiS/CdS) and beyond that point, NiS aggregates will cause faster recombination and thereby poorer photocatalytic performance of the NiS/CdS nanocomposites.

3.5. Mechanism for the photocatalytic hydrogen evolution

Based on all the above discussion, a model is putted forward to explain the mechanism of the overall HER reactions, as shown in Fig. 13. Electrons and holes are first generated in CdS when it is excited with light ($\lambda \geq 400$ nm). Although the CB edge of CdS is more negative than the reduction potential of H^+/H_2, the rate of hydrogen evolution is low over pure CdS because of the fast recombination of photoinduced charge carriers. When NiS nanoparticles are loaded on the surface of CdS, due to the less negative CB of NiS than that of CdS, the photogenerated electrons in the CB of CdS can be transferred to NiS nanoparticles. More importantly, the intimate interfacial junction between NiS and CdS plays an essential role in facilitating electron transmit from CdS to NiS. The NiS also acts as active sites because unsaturated sulfide ions of NiS possess strong affinity for H^+ in the solution and can thus enhance the photocatalytic performance. The photoinduced holes in the VB of CdS can oxidize hole scavengers, described by the pathway I/II in Fig. 13. When only the lactic acid acts as sacrificial agent, the holes can
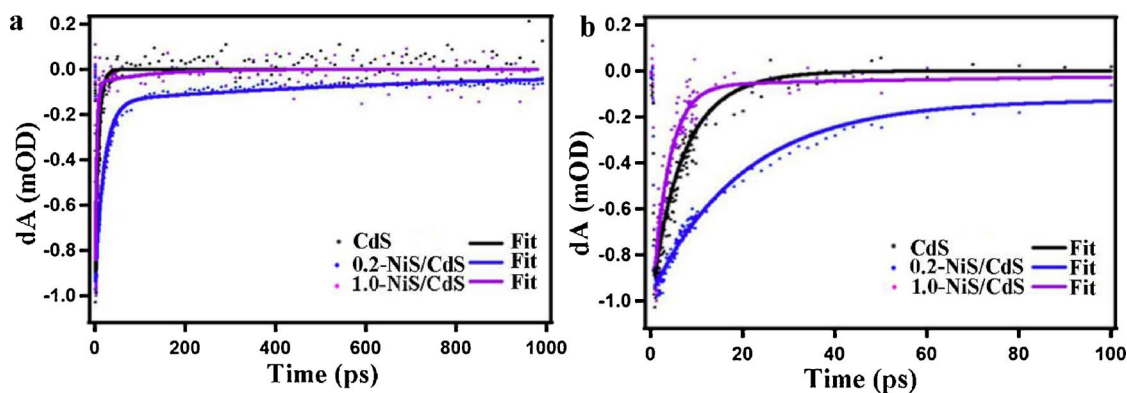
Fig. 12. Normlized ultrafast transient bleach decay profile of CdS nanowire (black), 0.2-NiS/CdS (blue) and 1.0-NiS/CdS (purple). The decay profiles are fitted using a double exponential function. (For interpretation of the references to colour in this figure legend, the reader is referred to the web version of this article.)

Table 1
Fitting parameters of transient bleach recovery of CdS, 0.2-NiS/CdS and 1.0-NiS/CdS fitted with double exponential function and calculated average lifetime (τ).

Sample	A_1	τ_1 (ps)	A_2	τ_2 (ps)	Average τ (ps)
CdS	0.72	8.8 ± 0.4	0.28	3.6 ± 0.1	8
0.2-NiS/CdS	0.83	20.0 ± 0.1	0.14	879 ± 17	776
1.0-NiS/CdS	0.94	3.5 ± 0.1	0.05	117 ± 9	76

be just consumed by the one substance (pathway I). While taking the lignin as an additional hole scavenger, it will produce methanol, ethanol, formaldehyde, formic acid and oxalic acid during the HER process, which provides an extra pathway for reaction of the holes (pathway II). The fast consumption of the holes can greatly inhibit recombination of the electron and hole, thereby suppressing the photocorrosion of CdS and enhancing the H_2 evolution rate. The results suggest that reaction of the hole is a rate limiting step in the overall photocatalytic reactions.

4. Conclusion

In summary, 1D NiS/CdS nanocomposites with different NiS loading have been synthesized using a two-step solvothermal method. Morphological and structural analyses showed that NiS and CdS have close interfacial contact. The photocatalytic H_2 evolution activity of NiS/CdS nanocomposites exhibited a significant improvement compared to pristine CdS. The 0.2-NiS/CdS nanocomposite showed the

highest hydrogen production rate of 1512.4 μmol h^{-1} g^{-1} with lactic acid and lignin as the hole scavenger, corresponding to a AQE of 44.9%, which was approximately 554 times higher than that of pristine CdS NWs. This result can be attributed to efficient charge separation at the interfaces between CdS and NiS, suppressing electron-hole recombination within CdS. Furthermore, stability study showed that the optimized sample (0.2-NiS/CdS) was highly stable.

To gain deeper insight into the enhancement mechanism behind, charge carrier dynamics of pure CdS and NiS/CdS nanocomposites were investigated employing ultrafast laser spectroscopy. The 0.2-NiS/CdS nanocomposite showed a much longer average charge carrier lifetime than pure CdS and NiS/CdS nanocomposites with higher NiS loading. Longer charger carrier lifetime seems to correspond with better photocatalytic performance of the catalysts, which is often expected as longer-lived charge carriers will have a better chance for participating in redox reactions rather than recombining. Together, this work demonstrated a simple strategy for designing and constructing highly efficient, environmental friendly, low cost, and non-noble-metal photocatalysts for hydrogen generation. The use of biomass in the reactions provides additional benefit to this approach.
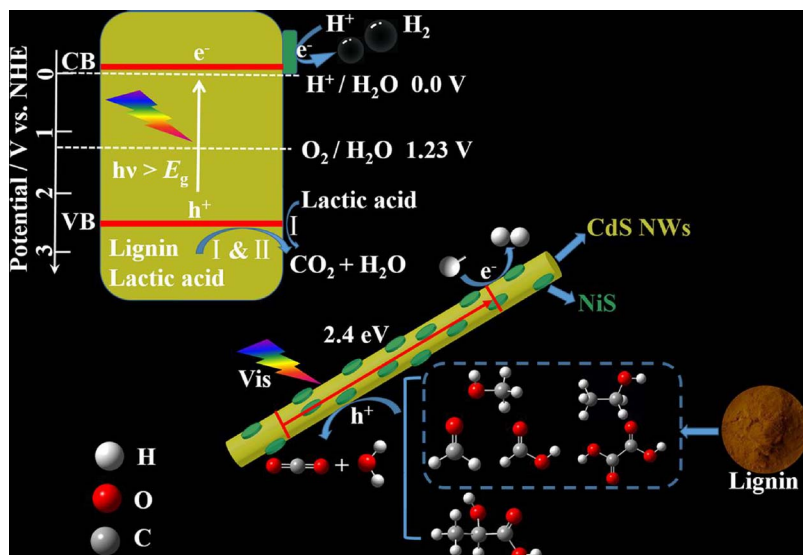
Fig. 13. Scheme for the photocatalytic hydrogen production over NiS/CdS nanocomposites under visible light.

Appendix A. Supplementary data

Supplementary data associated with this article can be found, in the online version, at https://doi.org/10.1016/j.apcatb.2018.01.038.

References

[1] R.D. Cortright, R.R. Davda, J.A. Dumesic, Hydrogen from catalytic reforming of biomass-derived hydrocarbons in liquid water, Nature 418 (2002) 964–967.

[2] Y.L. Chen, G.T. Yu, W. Chen, Y.P. Liu, G.D. Li, P.W. Zhu, Q. Tao, Q.J. Li, J.W. Liu, X.P. Shen, H. Li, X.R. Huang, D.J. Wang, T. Asefa, X.X. Zou, Highly active, non-precious electrocatalyst comprising borophene subunits for the hydrogen evolution reaction, J. Am. Soc. 139 (2017) 12370–12373.

[3] L. Ma, H. Fan, M. Li, H. Tian, J. Fang, G. Dong, A simple melamine-assisted exfoliation of polymeric graphitic carbon nitrides for highly efficient hydrogen production from water under visible light, J. Mater. Chem. A 3 (2015) 22404–22412.

[4] C.W. Zhao, Y.A. Li, X.R. Wang, G.J. Chen, Q.K. Liu, J.P. Ma, Y.B. Dong, Fabrication of Cd(II)-MOF-based ternary photocatalytic nanocomposite materials for H_2 production via a gel-to-crystal approach, Chem. Commun. 51 (2015) 15906–15909.

[5] D.R. Sun, L. Ye, Z.H. Li, Visible-light-assisted aerobic photocatalytic oxidation of amines to imines over NH_2-MIL-125(Ti), Appl. Catal. B Environ. 164 (2015) 428–432.

[6] Y.J. Yuan, Z.J. Ye, H.W. Lu, B. Hu, Y.H. Li, D.Q. Chen, J.S. Zhong, Z.T. Yu, Z.G. Zou, Constructing anatase TiO_2 nanosheets with exposed (001) facets/layered MoS_2 two-dimensional nanojunctions for enhanced solar hydrogen generation, ACS Catal. 6 (2016) 532–541.

[7] X.W. Wang, G. Liu, Z.G. Chen, F. Li, L.Z. Wang, G.Q. Lu, H.M. Cheng, Enhanced photocatalytic hydrogen evolution by prolonging the lifetime of carriers in ZnO/CdS heterostructures, Chem. Commun. (2009) 3452–3454.

[8] J. Jin, J.G. Yu, G. Liu, P.K. Wong, Single crystal CdS nanowires with high visible-light photocatalytic H_2-production performance, J. Mater. Chem. A 1 (2013) 10927–10934.

[9] J. Zhang, Y. Wang, J. Jin, J. Zhang, Z. Lin, F. Huang, J. Yu, Efficient visible-light photocatalytic hydrogen evolution and enhanced photostability of core/shell CdS/g-C_3N_4 nanowires, ACS Appl. Mater. Interfaces 5 (2013) 10317–10324.

[10] D. Yue, X. Qian, M. Kan, M. Ren, Y. Zhao, Sulfurated [NiFe]-based layered double hydroxides nanoparticles as efficient co-catalysts for photocatalytic hydrogen evolution using CdTe/CdS quantum dots, Appl. Catal. B Environ. 209 (2017) 155–160.

[11] D. Yue, X. Qian, Z. Zhang, M. Kan, M. Ren, Y. Zhao, CdTe/CdS Core/Shell quantum dots cocatalyzed by sulfur tolerant [Mo3S13]2 − nanoclusters for efficient visible-light-driven hydrogen evolution, ACS Sustain. Chem. Eng. 4 (2016) 6653–6658.

[12] X.L. Yin, L.L. Li, W.J. Jiang, Y. Zhang, X. Zhang, L.J. Wan, J.S. Hu, MoS_2/CdS nanosheets-on-nanorod heterostructure for highly efficient photocatalytic H_2 generation under visible light irradiation, ACS Appl. Mater. Interfaces 8 (2016) 15258–15266.

[13] W.G. Jiang, Y.F. Liu, R.L. Zong, Z.P. Li, W.Q. Yao, Y.F. Zhu, Photocatalytic hydrogen generation on bifunctional ternary heterostructured In_2S_3/MoS_2/CdS nanocomposites with high activity and stability under visible light irradiation, J. Mater. Chem. A 3 (2015) 18406–18412.

[14] J.Z. Chen, X.J. Wu, L.S. Yin, B. Li, X. Hong, Z.X. Fan, B. Chen, C. Xue, H. Zhang, One-pot synthesis of CdS nanocrystals hybridized with single-layer transition-metal dichalcogenide nanosheets for efficient photocatalytic hydrogen evolution, Angew. Chem. Int. Ed. 54 (2015) 1210–1214.

[15] J. He, L. Chen, F. Wang, Y. Liu, P. Chen, C.T. Au, S.F. Yin, CdS nanowires decorated with ultrathin MoS_2 nanosheets as an efficient photocatalyst for hydrogen evolution, ChemSusChem 9 (2016) 624–630.

[16] X. Zong, H.J. Yan, G. Wu, G.P. Ma, F.Y. Wen, L. Wang, C. Li, Enhancement of photocatalytic H_2 evolution on CdS by loading MoS_2 as cocatalyst under visible light irradiation, J. Am. Chem. Soc. 130 (2008) 7176–7177.

[17] J. Zhang, J.G. Yu, M. Jaroniec, J.R. Gong, Noble metal-free reduced graphene Oxide-$Zn_xCd_{1-x}S$ nanonanocomposite with enhanced solar photocatalytic H_2-production performance, Nano Lett. 12 (2012) 4584–4589.

[18] J.G. Yu, J. Zhang, M. Jaroniec, Preparation and enhanced visible-light photocatalytic H_2-production activity of CdS quantum dots-sensitized $Zn_{1-x}Cd_xS$ solid solution, Green Chem. 12 (2010) 1611–1614.

[19] Y.B. Wang, Y.S. Wang, R. Xu, Photochemical deposition of pt on CdS for H_2 evolution from water: markedly enhanced activity by controlling Pt reduction environment, J. Phys. Chem. C 117 (2013) 783–790.

[20] H. Park, W. Choi, M.R. Hoffmann, Effects of the preparation method of the ternary CdS/TiO_2/Pt hybrid photocatalysts on visible-light-induced hydrogen production, J. Mater. Chem. 18 (2008) 2379–2385.

[21] H.J. Yan, J.H. Yang, G.J. Ma, G.P. Wu, X. Zong, Z.B. Lei, J.Y. Shi, C. li, Visible-light-driven hydrogen production with extremely high quantum efficiency on Pt–PdS/CdS photocatalyst, J. Catal. 266 (2009) 165–168.

[22] C.V. Thulasi-varma, C.V.V.M. Gopi, S.S. Rao, D. Punnoose, S.K. Kim, H.J. Kim, Time varied morphology controllable fabrication of NiS nanosheets structured thin film and its application as a counter electrode for QDSSC, J. Phys. Chem. C 119 (2015) 11419–11429.

[23] X. Sun, J. Dou, F.Y. Xie, Y.F. Li, M.D. Wei, One-step preparation of mirror-like NiS nanosheets on ITO for the efficient counter electrode of dye-sensitized solar cells, Chem. Commun. 50 (2014) 9869–9871.

[24] L. Zhang, B.Z. Tian, F. Chen, J.L. Zhang, Nickel sulfide as co-catalyst on nanostructured TiO_2 for photocatalytic hydrogen evolution, Int. J. Hydrogen Energy 37 (2012) 17060–17067.

[25] Z.H. Chen, P. Sun, B. Fan, Z.G. Zhang, X.M. Fang, In situ template-free ion-exchange process to prepare visible-light-active g-C_3N_4/NiS hybrid photocatalysts with enhanced hydrogen evolution activity, J. Phys. Chem. C 118 (2014) 7801–7807.

[26] W. Zhang, Y.B. Wang, Z. Wang, Z.Y. Zhong, R. Xu, Highly efficient and noble metal-free NiS/CdS photocatalysts for H_2 evolution from lactic acid sacrificial solution under visible light, Chem. Commun. 46 (2010) 7631–7633.

[27] J. Zhang, S.Z. Qiao, L.F. Qi, J.Q. Yu, Fabrication of NiS modified CdS nanorod p–n junction photocatalysts with enhanced visible-light photocatalytic H_2-production activity, Phys. Chem. Chem. Phys. 15 (2013) 12088–12094.

[28] M. Bowker, Sustainable hydrogen production by the application of ambient temperature photocatalysis, Green Chem. 13 (2011) 2235–2246.

[29] M. Bowker, L. Millard, J. Greaves, D. James, J. Soares, Photocatalysis by Au nanoparticles: reforming of methanol, Gold Bull. 37 (2004) 170–173.

[30] J. Mock, Y. Zheng, A.P. Mueller, S. Ly, L. Tran, S. Segovia, M. Nagaraju, M. Köpke, P. Dürre, R.K. Thauer, Energy conservation associated with ethanol formation from H_2 and CO_2 in clostridium autoethanogenum involving electron bifurcation, J. Bacteriol. 197 (2015) 2965–2980.

[31] M. Bowker, P.R. Davies, L.S. Al-mazroai, Photocatalytic reforming of glycerol over gold and palladium as an alternative fuel source, Catal. Lett. 128 (2009) 253–255.

[32] P. Mäki-Arvela, B. Holmbom, B. Holmbom, T. Salmi, D.Y. Murzin, Recent progress in synthesis of fine and specialty chemicals from wood and other biomass by recent progress in synthesis of fine and specialty chemicals from wood and other biomass by heterogeneous catalytic processes, Catal. Rev. 49 (2007) 197–340.

[33] S. Shen, P. Guo, D.A. Wheeler, J. Jiang, S.A. Lindley, C.X. Kronawitter, J.Z. Zhang, S.S. Mao, Physical and photoelectrochemical properties of Zr-doped hematite nanorod arrays, Nanoscale 5 (2013) 9867–9874.

[34] W. Zhang, Y.B. Wang, Z. Wang, Z.Y. Zhong, R. Xu, Highly efficient and noble metal-free NiS/CdS photocatalysts for H_2 evolution from lactic acid sacrificial solution under visible light, Chem. Commun. 46 (2010) 7631–7633.

[35] Q.Z. Wang, J.H. Lian, J.J. Li, R.F. Wang, H.H. Huang, B.T. Su, Z.Q. Lei, Highly efficient photocatalytic hydrogen production of flower-like cadmium sulfide decorated by histidine, Sci. Rep. 5 (13593) (2015) 1–9.

[36] C.H. Li, H.M. Wang, D.Z. Lu, W.H. Wu, J.Q. Ding, X.N. Zhao, R.Y. Xiong, M.C. Yang, P. Wu, F.T. Chen, P.F. Fang, Visible-light-driven water splitting from dyeing wastewater using Pt surface-dispersed TiO_2-based nanosheets, J. Alloys Compd. 699 (2017) 183–192.

[37] C.H. Li, H.M. Wang, J.L. Ming, M. Liu, P.F. Fang, Hydrogen generation by photocatalytic reforming of glucose with heterostructured CdS/MoS_2 nanocomposites under visible light irradiation, Int. J. Hydrogen Energy 42 (2017) 16968–16978.

[38] J. Xu, X.J. Cao, Characterization and mechanism of MoS_2/CdS nanocomposite photocatalyst used for hydrogen production from water splitting under visible light, Chem. Eng. J. 260 (2015) 642–648.

[39] J.L. Meng, Z.M. Yu, Y. Li, Y.D. Li, PdS-modified CdS/NiS nanocomposite as an efficient photocatalyst for H_2 evolution in visible light, Catal. Today 225 (2014) 136–141.

[40] B. Han, S.Q. Liu, N. Zhang, Y.J. Xu, Z.R. Tang, One-dimensional CdS@MoS_2 core-shell nanowires for boosted photocatalytic hydrogen evolution under visible light, Appl. Catal. B Environ. 202 (20176) (2016) 298–304.

[41] L. Yang, X. Zhu, S. Xiong, X. Wu, Y. Shan, P.K. Chu, Synergistic $WO_3 \cdot 2H_2O$ Nanoplates/WS_2 hybrid catalysts for high-efficiency hydrogen evolution, ACS Appl. Mat. Interfaces 8 (2016) 13966–13972.

[42] N. Qin, J. Xiong, R. Liang, Y. Liu, S. Zhang, Y. Li, Highly efficient photocatalytic H_2 evolution over MoS_2/CdS-TiO_2 nanofibers prepared by an electrospinning mediated photodeposition method, Appl. Catal. B Environ. 202 (2017) 374–380.

[43] N. Jiang, Q. Tang, M.L. Sheng, B. You, D.E. Jiang, Y.J. Sun, Nickle sulfides for electrocatalytic hydrogen evolution under alkaline conditions: a case study of crystalline NiS, NiS_2, and Ni_3S_2 nanoparticles, Catal. Sci. Technol. 6 (2016) 1077–1084.

[44] J.S. Chen, J. Ren, M. Shalon, T. Fellinger, M. Antonietti, Stainless steel mesh-supported NiS nanosheet array as highly efficient catalyst for oxygen evolution reaction, ACS Appl. Mater. Interfaces 8 (2016) 5509–5516.

[45] J. Xu, X.J. Cao, Characterization and mechanism of MoS_2/CdS nanocomposite photocatalyst used for hydrogen production from water splitting under visible light, Chem. Eng. J. 260 (2015) 642–648.

[46] Y.J. Yuan, F. Wang, B. Hu, H.W. Lu, Z.T. Yu, Z.G. Zou, Significant enhancement in photocatalytic hydrogen evolution from water using a MoS_2 nanosheet-coated ZnO heterostructure photocatalyst, Dalton Trans. 44 (2015) 10997–11003.

[47] L.J. Shen, M.B. Luo, Y.H. Liu, R.W. Liang, F.F. Jing, L. Wu, Noble-metal-free MoS_2 co-catalyst decorated UiO-66/CdS hybrids for efficient photocatalytic H_2 production, Appl. Catal. B Environ. 166–167 (2016) 445–453.

[48] S.R. Kadam, V.R. Mate, R.P. Panmand, L.K. Nikam, M.V. Kulkarni, R.S. Sonawane, B.B. Kale, A green process for efficient lignin (biomass) degradation and hydrogen production via water splitting using nanostructured C, N S-doped ZnO under solar light, RSC Adv. 4 (2014) 60626–60635.

[49] K. Kobayakawa, Y. Sato, S. Nakamura, A. Fujishima, Photodecomposition of Kraft lignin catalyzed by titanium dioxide, Bull. Chem. Soc. Jpn. 62 (1989) 3433–3436.

[50] H. Ohnishi, H. Matsumura, H. Tsubomura, M. Iwasaki, Bleaching of lignin solution by a photocatalyzed reaction on semiconductor photocatalysts, Ind. Eng. Chem. Res. 28 (1989) 719–724.

[51] J. Zhang, L.H. Wang, X.H. Liu, X.A. Li, W. Huang, High-performance CdS–ZnS core–shell nanorod array photoelectrode for photoelectrochemical hydrogen

generation, J. Mater. Chem. A 3 (2015) 535–541.

[52] K.L. He, J. Xie, Z.H. Yang, R.C. Shen, Y.P. Fang, S. Ma, X.B. Chen, X. Li, Earth-abundant WC nanoparticles as an active noble-metal-free co-catalyst for the highly boosted photocatalytic H_2 production over g-C_3N_4 nanosheets under visible light, Catal. Sci. Technol. 7 (2017) 1193–1202.

[53] G.S. Li, L. Wu, F. Li, P.P. Xu, D.Q. Zhang, H.X. Li, Photoelectrocatalytic degradation of organic pollutants via a CdS quantum dots enhanced TiO_2 nanotube electrode under visible light irradiation, Nanoscale 5 (2013) 2118–2125.

[54] Z.M. Bai, X.Q. Yan, Y. Li, Z. Kang, S.Y. Cao, Y. Zhang, 3D-Branched ZnO/CdS na-nowire arrays for solar water splitting and the service safety research, Adv. Energy Mater. 6 (1501459) (2016) 1–8.

[55] S.R. Sun, L. Gao, Y.Q. Liu, Enhanced dye-sensitized solar cell using graphene-TiO_2 photoanode prepared by heterogeneous coagulation, Appl. Phys. Lett. 96 (83113) (2013) 1–3.

[56] L.T. Ma, H.Q. Fan, J. Wang, Y.W. Zhao, H.L. Tian, G.Z. Dong, Water-assisted ions in situ intercalation for porous polymeric graphitic carbon nitride nanosheets with superior photocatalytic hydrogen evolution performance, Appl. Catal. B Environ.

190 (2016) 93–102.

[57] J.W. Fang, H.Q. Fan, M.M. Li, C.B. Long, Nitrogen self-doped graphitic carbon ni-tride as efficient visible light photocatalyst for hydrogen evolution, J. Mater. Chem. A 3 (2015) 13819–13826.

[58] S.C. Han, Y.C. Pu, L.X. Zheng, J.Z. Zhang, X.S. Fang, Shell-thickness dependent electron transfer and relaxation in type-II core–shell CdS/TiO_2 structures with op-timized photoelectrochemical performance, J. Mater. Chem. A 3 (2015) 22627–22635.

[59] D.A. Wheeler, J.Z. Zhang, Exciton dynamics in semiconductor nanocrystals, Adv. Mater. 25 (2013) 2878–2896.

[60] C. Burda, S. Link, M.B. Mohamed, M. El-sayed, C. Burda, S. Link, M.B. Mohamed, M. El-sayed, The pump power dependence of the femtosecond relaxation of CdSe nanoparticles observed in the spectral range from visible to infrared, J. Chem. Phys. 116 (2002) 3828–3833.

[61] J.K. Cooper, Y.C. Ling, C. Longo, Y. Li, J.Z. Zhang, Effects of hydrogen treatment and air annealing on ultrafast charge carrier dynamics in ZnO nanowires under in situ photoelectrochemical conditions, J. Phys. Chem. C 116 (2012) 17360–17368.